Chapter 4

Guidelines for the rational design of nickel – based double hydroxide electrocatalysts for the oxygen evolution reaction

ABSTRACT

The oxygen evolution reaction (OER) is one of the major bottlenecks hindering the implementation of a global economy based on solar fuels. The current limitations may only be overcome with cost-effective, active and stable electrocatalysts. It is known that Ni-based catalysts exhibit remarkable catalytic activities for the OER in alkaline media. In this joint theoretical-experimental study, we provide a thorough characterization of Ni-based double hydroxides with Cr, Mn, Fe, Co, Cu and Zn at the atomic scale that not only explains the reasons for their high activity but also provides simple design principles for the enhancement of their electrocatalytic properties. Our approach, based on the local symmetry and composition of the active sites, helps rationalize the effect of dopants on the catalytic activity of $Ni(OH)_2$ and, particularly, gives insights of the different roles of iron, chromium and manganese in the superior catalytic activity of NiFe, NiCr and NiMn double hydroxides, which reduce the OER potential to reach 0.5 mA cm^{-2} by 230 mV, 190 mV and 160 mV compared to IrO_2 nanoparticles, the state-of-the-art benchmarking catalysts, with 90% Faradaic efficiency for O_2 generation.

The content of this chapter has been published in: Diaz-Morales, O.; Ledezma-Yanez, I.; Koper, M.T.M. and Calle-Vallejo, F. *ACS Catalysis* **2015**, 5, 5380-5387

4.1. Introduction

Fossil fuels have played a central role in the development of society since the beginning of the industrial revolution in the 18th century, powering factories and related technologies and transportation networks that drive and sustain modern civilization. However, the world population has tremendously increased since then, with the concomitant increase in energy needs.[1] This has turned the availability of fossil fuels into an issue for future generations. Besides, combustion of fossil fuels is environmentally harmful and is responsible for serious public health problems related to the reduction of air quality.[1-3] Furthermore, recent studies suggest that the increase of the global average temperature should not exceed 2 °C, which may only be achieved by drastic reductions of CO_2 emissions associated to burning coal, oil and natural gas, added to the widespread use of alternative sources of energy.[4] Among those, sunlight is by far the largest exploitable resource.[5] The transformation of solar energy into chemical energy is promising,[3,5-7] as the electrons generated by (photo)-electrochemical oxygen evolution can be used to drive, for instance, the electrochemical reduction of protons or carbon dioxide into fuels. An additional benefit of such process is that water and oxygen are the main byproducts.

Nevertheless, one of the major bottlenecks hampering the application of solar power as a widespread energy source is the slow kinetics of oxygen evolution reaction (OER). The overpotential of this reaction reduces significantly the overall efficiency of energy conversion.[8,9] Numerous catalysts have been studied to accelerate the water oxidation reaction but the most active compounds are based on scarce, hence expensive compounds such as IrO_2 or RuO_2.[10-12] Alternatively, catalysts based on earth-abundant transition metals have been proposed, showing comparable and even higher intrinsic activity towards OER in alkaline media than the iridium or ruthenium-based catalysts.[9,12-17] Those catalysts are mainly based on nickel or cobalt oxides, the activity of which has been rationalized through DFT calculations.[14,18]

Materials based on nickel hydroxide have also been studied, displaying good catalytic activity for oxygen evolution in alkaline media.[13,15,17,19-21] It has been reported that the catalytic activity of nickel hydroxide can be significantly enhanced by modifying it with

other transition metals like chromium or iron,[13,20-22] and the intrinsic catalytic activity of NiFe double hydroxides (from here on DHs) towards oxygen evolution in alkaline media has been shown to be considerably higher than that of iridium-based catalysts.[15,17,23,24] However, there are no systematic attempts to understand the correlation between the activity of nickel-based double hydroxides towards water oxidation and the nature of the added transition metals. Furthermore, comparison between different literature reports on the experimental activity of DHs is not straightforward due to the differences in the way of benchmarking the catalytic activity.[15,21]

We present here a theoretical and experimental study of the electrocatalytic properties of nickel-based double hydroxides with 3d transition metals for the OER in alkaline media. This work gives a systematic study of the effect of transition-metal doping on the activity of nickel-based catalysts. The joint analysis of theoretical and experimental results is generally more accurate and insightful when multiple materials are compared,[18,25] which is why we have established some theoretical trends in catalytic activity for a given family of compounds, synthesized all of them by means of the same method and measured their experimental activities in identical conditions. The trends are rationalized in terms of the local symmetry and composition of the active sites, and aim at providing simple and general design rules in OER electrocatalysis.

4.2. Computational and Experimental Details

4.2.1. DFT calculations

The DFT calculations were performed with the Vienna ab initio simulation package,[26] using the RPBE exchange-correlation functional[27] and ultrasoft pseudopotentials.[28] Such functional and pseudopotentials allow for straightforward comparisons with previous works.[18] The simulations were made with 4-layer slabs: the two top layers were free to move in all directions, while the two bottom layers were fixed at the ground-state bulk distances. The relaxations were carried out with the quasi-Newton scheme for the using as convergence criterion a maximum residual force on any atom of 0.05 eV $Å^{-1}$. In the low-coverage calculations the adsorbates were free to move in all directions, while in certain

high-coverage calculations the x or y directions were constrained. The simulated 2×2 (001) monoxide slabs with a $4 \times 4 \times 1$ k-point mesh and a plane-wave cutoff of 450 eV ensured convergence of the adsorption energies within 0.05 eV. The monoxides were simulated in the rock salt structure. We added 15 Å of vacuum between periodically repeated images and applied dipole corrections. The Methfessel-Paxton method was used to smear the Fermi level[29] with $k_BT = 0.1$ eV, and all energies were extrapolated to 0 K. The gas-phase molecules (H_2, H_2O) were calculated in boxes of 15 Å × 15 Å × 15 Å, $k_BT = 0.001$ eV and a $1 \times 1 \times 1$ k-point mesh. The free energies are approximated as follows: $G = E_{DFT} + ZPE - TS$, where E_{DFT} and ZPE are the total and zero-point electronic energies calculated through DFT, and TS are entropic contributions (only taken into account for gas-phase species). The ZPEs in eV for H_2, H_2O, *O, *OH and *OOH are, respectively, 0.27, 0.56, 0.07, 0.34 and 0.40. The TS corrections in eV for H_2 and $H_2O_{(l)}$ are 0.40 and 0.67 eV,[30,31] respectively. In order to describe the energetics of solvated protons and electrons and to estimate overpotentials we used the computational hydrogen electrode.[31] The procedure for estimating the free energies of adsorption of *O, *OH and *OOH, which are the considered oxygen evolution intermediates, a brief discussion on solvation and the details of the construction of the volcano plots are given in Appendix C and have also been given elsewhere.[18,30] The active sites on the (001) facet are illustrated in Figure 1. The (001) surfaces of the monoxides (MO with M = Ca to Cu) were initially simulated (Figure 1a). Furthermore, the surface layer of a NiO substrate was partially hydrogenated and doped with Cr, Mn, Fe, Co, Ni, Cu and Zn (Figure 1b), so as to model oxyhydroxide (NiMOOH) sites. To date, there are no clear conclusions in the literature about the actual surface morphology of Ni (oxy)hydroxides with and without Fe doping. This holds for theoretical as well as experimental studies. In fact, various authors have claimed that under reaction conditions, different oxyhydroxide phases compose the exposed surfaces. For instance, Bell and coworkers[24] claim that Fe doping enhances the activity of the (0 1 -1 2) plane of γ-NiOOH, while Li and Selloni[32] attribute the activity to the (0 1 -1 5) plane of β-NiOOH.

In any case, the EXAFS experiments of Bell and coworkers[24] reveal valuable information: both metals in NiFeOOH form octahedral complexes of the type NiO_6 and FeO_6. This is the reason why we have used bulk nickel monoxide (NiO) to build our

surfaces, as it contains octahedral metal centers surrounded by six oxygen ligands (NiO_6). Moreover, we have hydrated one of the surface oxygen atoms and doped with Cr, Mn, Fe, Co, Ni, Cu and Zn (Figure 1b) so that the composition of the top layer of a 2×2 unit cell is NiMOOH. In that way, we can reproduce in our model the only two certain experimental observations of Ni oxides under OER conditions: i) the surface is partially dehydrated, so that hydroxides turn into oxyhydroxides. ii) The metal centers form MO_6 and NiO_6 complexes. In broad terms, the use of hydrogenated NiO is as arbitrary as the use of γ-NiOOH or β-NiOOH until further conclusive experimental evidence is obtained. This choice ensures, therefore, that the local symmetry of the catalyst is reproduced, in spite of the lack of precise information on the catalyst's surface morphology. The OER activity of these sites was modeled at a high coverage of oxygenated species (see Figure 1c and full details in Appendix C, Figure C7) and all calculations were spin-unrestricted. For each system, ferromagnetic and antiferromagnetic calculations (with spin alignment planes on the (111) and (100) planes) were carried out. Note that MnO, FeO, CoO and NiO are antiferromagnetic oxides. Particularly, NiO has spin alignment in the (111) plane.[24]

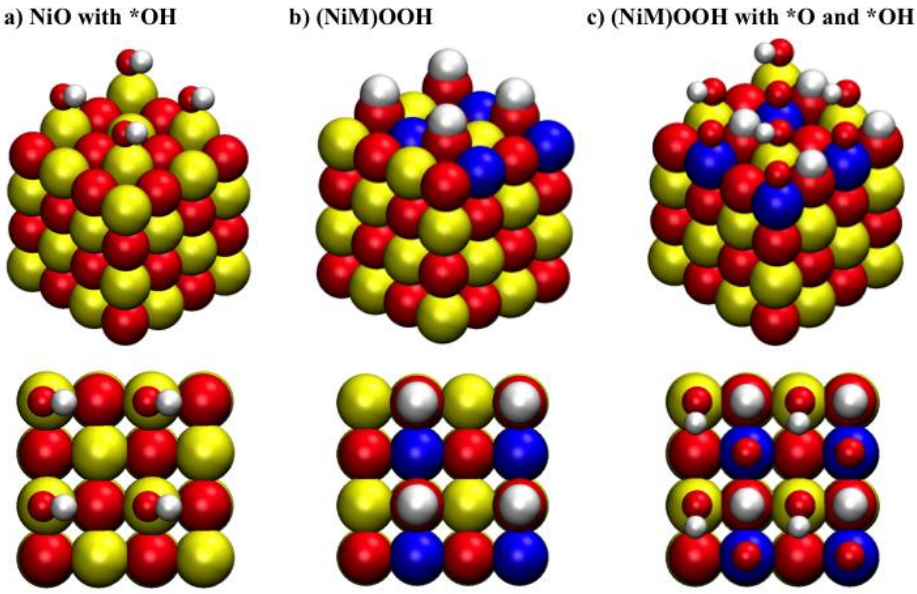

Figure 1. Perspective and top views of the active sites at (001) surface facets of the oxides under study. In this surface facet, octahedral NiO_6 and MO_6 complexes are formed. Ni atoms appear in yellow, oxygen atoms in red, M atoms in blue, where M can be Cr, Mn, Fe, Co, Ni, Cu and Zn; and H atoms in white. For convenience, O and H atoms in the lattice (large) and adsorbed (small) have been drawn with different radii. a) NiO with *OH adsorbed on Ni. b) Clean NiMOOH. This structure contains 50% M in the top layer and one of the oxygen atoms has been hydrogenated. c) The same as in b) with *O on M and *OH on Ni, corresponding to the active sites under OER conditions.

4.2.2. Chemicals

The following reagents were utilized: $Ni(NO_3)_2{\cdot}6H_2O$ (Sigma-Aldrich, purum p.a., crystallized, ≥97.0% (KT)), $Cr(NO_3)_3{\cdot}9H_2O$ (Sigma-Aldrich, puriss. p.a., ≥98.0%), $Mn(NO_3)_2{\cdot}xH_2O$ (Alfa Aesar, metal basis, ≥97.0%), $CoCl_2{\cdot}6H_2O$ (Sigma-Aldrich, purum p.a., crystallized, ≥98.0% (KT)), $Fe(NO_3)_3{\cdot}9H_2O$ (Sigma-Aldrich, ACS reagent, ≥98%), $Cu(NO_3)_2{\cdot}3H_2O$ (Sigma-Aldrich, purum p.a., 98.0-103% (KT)), $Zn(NO_3)_2{\cdot}6H_2O$ (Sigma-Aldrich, reagent grade, 980%), $Na_2CO_3{\cdot}10H_2O$ (Merck, pro analysis), KOH (Sigma-Aldrich, semiconductor grade, pellets, 99.99% trace metals basis), EtOH (Sigma-Aldrich,

puriss. p.a., absolute, ≥99.8% (GC)). Nafion® (Sigma-Aldrich, 5 wt. % in lower aliphatic alcohols and 15-20% water). All chemicals were used as received, unless otherwise stated. The water used in all experiments was deionized and ultrafiltrated by a Millipore Milli-Q system (resistivity > 18.2 MΩ cm and TOC < 5ppb).

4.2.3. Cleaning procedure

The glassware was thoroughly cleaned before the experiments by boiling in a 1:3 mixture of concentrated HNO_3/concentrated H_2SO_4 to remove organic contaminations. After this initial treatment, the glassware was boiled five times in water. When not in use, it was stored in an aqueous solution of 0.5 M H_2SO_4 and 1 g/L $KMnO_4$. To remove the permanganate, the glassware was rinsed thoroughly with water and then immersed in a solution 1:1 of concentrated H_2SO_4 and 30% H_2O_2 to remove all particles of MnO_2. Afterwards, it was rinsed with water again and boiled five times in water.

4.2.4. Synthesis of the Nickel Double Hydroxides

All double hydroxides (DH) were prepared by the co-precipitation route[33], using 0.1 M solutions of $Ni(NO_3)_2$ and $M(NO_3)_n$ (M^{n+}= Cr^{3+}, Mn^{2+}, Fe^{3+}, Co^{2+}, Cu^{2+}, Zn^{2+}) as precursors. The precipitation was performed at 80 °C by dropping 32 mL of the solution with the metals in 1:1 molar ratio over 10 mL of water previously adjusted to pH 9 with 0.1 M Na_2CO_3. The pH was kept approximately constant at 9 during the synthesis by simultaneous dropping of 0.1 M Na_2CO_3 (36 mL). The addition of the Ni^{2+}/M^{n+} solution and the Na_2CO_3 was completed within 1.5 h, after which the suspension was glass-filtered and thoroughly rinsed with water. The powders were subsequently dried overnight at 120 °C and fine-ground.

Nickel(II) hydroxide was prepared by dropping 15 mL of NaOH 2M over 50 mL of $Ni(NO_3)_2$ 0.1 M. The suspension was glass-filtered and thoroughly rinsed with water. The powders were subsequently dried overnight at 120 °C and fine-ground.

4.2.5. Characterization

Powder X-Ray diffraction (XRD) measurements were performed in a Philips X'Pert diffractometer, equipped with the X'Celerator, using Cu-Kα radiation. The collection was done in the range $10° < 2\theta < 100°$ in steps of 0.020° (2θ) with counting time 10 s / step.

Fourier-transformed Infrared (FTIR) measurements were performed using an IRAffinity-1S FTIR spectrophotometer from Shimadzu. The machine is equipped with a high-energy ceramic light source, a temperature-controlled, high-sensitivity DLATGS detector, with a Michelson interferometer (30º incident angle) and a spectral resolution of 0.6 cm^{-1}.

Electrochemical measurements were carried out in a three-electrode, two-compartment cell with the reference electrode separated by a Luggin capillary. The working electrode over which the catalyst was supported was an Au rotating disk electrode (RDE) with a diameter of 4.6 mm, and all experiments were performed at 1500 RPM. The counter electrode was a gold spiral and a reversible hydrogen electrode (RHE) was used as reference electrode. Unless stated, all potentials in this work are referred to RHE scale. A platinum wire was connected to the reference electrode through a capacitor of 10 μF, acting as a low-pass filter to reduce the noise in the low current measurements. Electrochemical measurements were performed with a potentiostat PGSTAT12 (Metrohm - Autolab). Before and between measurements, the RDE electrode was first polished with 0.3 μm and 0.05 μm alumina paste (Buehler Limited). Subsequently, the electrode was ultrasonicated for 5 minutes in water to remove alumina particles. The OER measurements were conducted with cyclic voltammetry at 0.01 V s^{-1} in solutions saturated with Ar, bubbled at least 30 min prior to the electrochemical experiments.

The double hydroxides were immobilized on the electrode by drop-casting inks, using Nafion® as binder agent. We used Na-exchanged Nafion to avoid possible corrosion of the hydroxides due to the strong acidity of the commercially available solution. Alkaline Nafion was prepared according to the procedure reported in the literature,[34] by mixing 2 parts in volume of commercially available 5 wt.% Nafion solution with 1 part of 0.1 M

NaOH, which is reported to have ~ pH 11. The preparation of the inks is similar to previously reported methods to immobilize OER catalysts for RDE experiments,[35,36] with concentrations of 5 mg_{DH} mL_{ink}^{-1} and 1 mg_{Nafion} mL_{ink}^{-1}. The inks were prepared in absolute ethanol, first dispersing the DH within the solvent by sonication for 30 min, subsequently adding the Na-exchanged Nafion, followed by 20 min of further sonication. The catalysts were drop-casted on the Au disk to give a final loading of 75 μg_{DH} cm^{-2}_{disk} and dried in vacuum, where cm^2_{disk} accounts for the geometrical surface area of the disk.

The catalytic activity is reported as current density in mA cm_{oxide}^{-2}, where cm_{oxide}^{2} is the real surface area of the films, calculated from pseudo-capacitance measurements[12,37] in the potential region 0.9 – 1.0 V vs. RHE; the specific capacitance used for this measurement was 60 $\mu F \cdot cm^{-2}$.[37]

4.3. Results and Discussion

The advantageous catalytic[38] and electrocatalytic[10] properties of nickel-containing oxides are well documented. Particularly, recent theoretical studies[18,24,32,39] have shown the high activity of nickel-containing oxides for the OER. In those studies, NiO has been reported to have an activity close to optimal in Sabatier-type analyses. To confirm this observation, in Figure 2 we provide the calculated activities for the entire range of oxides between CaO and CuO. The descriptor used in the figure is the difference between the adsorption energies of *O and *OH, which is advantageous because it tunes simultaneously two adsorption energies (through their difference), instead of only one. Note that the existence of scaling relationships between *O, *OH and *OOH implies proportional variations of their differences.[40] Another advantage of this descriptor is that the points in the right leg of the volcano plot do not show scattering,[18] as evidenced in Figures 2 and 3. Alternatively, parameters different from adsorption energies have been used to describe activity trends on oxides, for instance bulk energetics,[41] and recent work has shown the correspondence between these parameters and adsorption energies.[39]

The trends in Figure 2 follow a volcano-shaped curve with the lowest overpotential corresponding to NiO. Additionally, MnO, CoO, FeO, and CuO are predicted to show fairly

high activities. However, it is not certain whether the active sites of these oxides under OER conditions correspond to those of the pristine oxide. For instance, the presence of oxyhydroxide phases at the potential and pH ranges of interest for the OER has been reported on Co, Ni and Au oxides.[32,42-44]

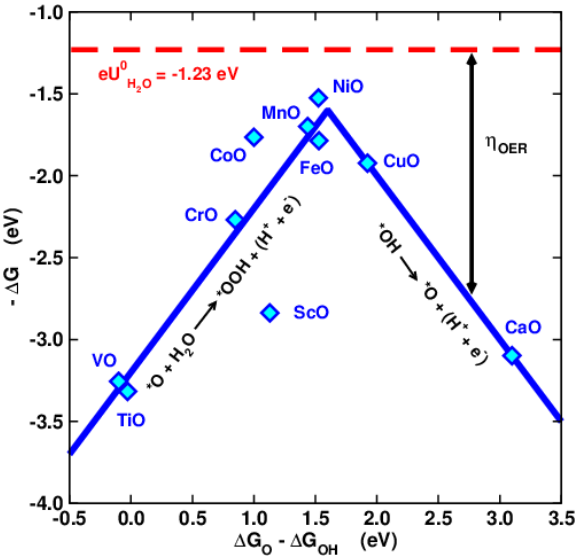

Figure 2. Sabatier-type volcano plot for the pristine (001) surfaces of the monoxides (see Figure 1a) in the range between CaO and CuO. The descriptor in the x-axis is the difference between the adsorption energies of oxygen and hydroxyl. The vertical differences between the red line and the blue lines and points provide an estimation of the oxygen evolution overpotential on the oxides. The potential-limiting steps are provided in black: the left leg of the volcano (strong binding side) is limited by the transformation of *O into *OOH, while the right leg (weak binding side) is limited by the transformation of *OH into *O (following ref.[18]).

Consequently, these observations set up an appropriate background to pose two important questions: first, is the pristine (001) surface with low-adsorbate coverage a good representation of NiO during the OER. Second, why is it possible to improve the activity of NiO by doping/mixing with other oxides, if NiO is already expected to be the most active monoxide? In the following we will address these questions both theoretically and experimentally and show that the answers are intimately related.

The descriptor in the x-axis in Figure 2, that is the difference between the adsorption energies of *O and *OH, marks the top of the activity plot at approximately 1.6 eV. Pristine NiO has a difference of ~1.5 eV, whence its low predicted overpotential. When the NiO surface is further oxidized and hydrated to produce active sites of the NiOOH type, the formal oxidation state of Ni changes from +2 to +3. This is reflected in a considerable weakening of the adsorption energies, so that the descriptor is ~1.84 eV for NiOOH. Note that similar decreases in binding strength have been reported for transition-metal oxides, including those of Ni, as the metal center is oxidized.[40] Hence, the value of the descriptor for pristine NiO is 0.1 eV more negative than required to be at the top of the volcano, whereas the value for the oxyhydroxide is 0.24 eV more positive than optimal. This difference of 0.24 eV from thermodynamic optimality suggests that significant improvements can be made to NiOOH-like active sites in terms of binding to OER intermediates. The design principle in this case is simple: NiOOH needs to be modified so that the difference in the adsorption energies of *O and *OH is decreased by approximately 0.24 eV.

We used this design criterion to assess the OER activity of NiMOOH sites with octahedral symmetry, with M = Cr, Mn, Fe, Co, Cu, and Zn. The results are shown in Figure 3, where NiOOH, NiO (from Figure 2) and IrO_2 (adapted from ref.[18]) are included for the sake of comparison. The figure includes the effect of doping on Ni sites and also the effect of the NiO lattice on the M sites. Figure 3a shows that the doping effects on Ni are modest, and slight increases on the OER overpotential with respect to NiOOH are observed for Mn, Fe, Co, Cu and Zn doping, while Cr doping decreases the overpotential. Thus, taking into account the accuracy of DFT at the GGA level, that is 0.2 eV,[45] it is possible to say that the predicted overpotentials of Ni sites in NiMOOH are similar to that of NiOOH, with only Cr doping reducing the overpotential, but the small differences make it hard to provide more detailed predictions. Note that although NiO is usually antiferromagnetic with spin alignment in the (111) plane,[24] the addition of dopants results in ferrimagnetic configurations and, in some cases, the spin alignments switch to the (100) plane. Therefore, the spin state of the surface is important for the determination of the trends.

On the other hand, the effects of the NiO lattice on the M sites are rather different, depending on the transition metals. Basically, there are two kinds of dopants in the studied group of transition metals: first, Mn and Fe, which possess nearly optimal binding energies and hence reduce the predicted OER overpotential; second, Cr, Co, Cu and Zn, which increase the OER overpotential.

In summary, the addition of Cr, Mn and Fe should enhance the OER activity of NiOOH, while Co, Cu and Zn will have similar or larger overpotentials than NiOOH.

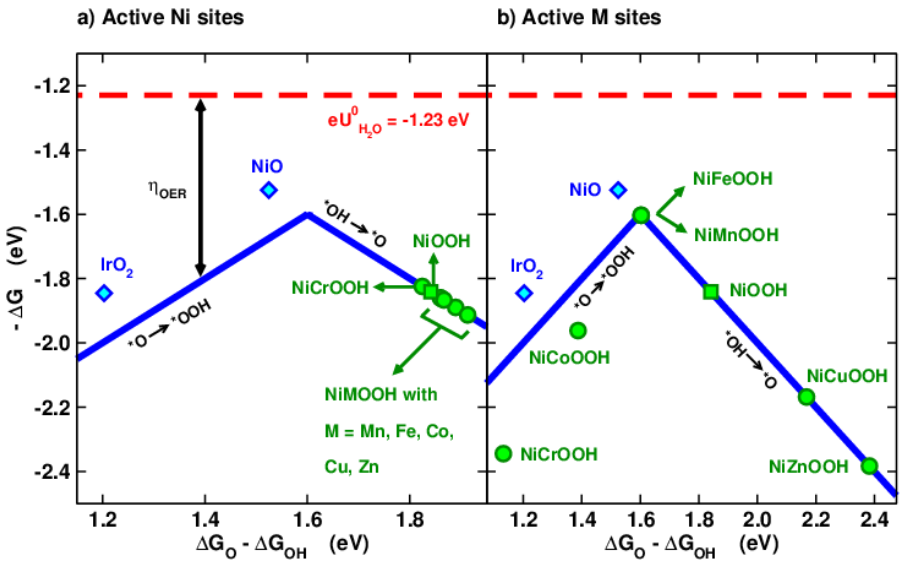

Figure 3. Sabatier-type volcano plots for Ni-based oxyhydroxide sites doped with transition metals (see Figures 1b and 1c). The surfaces were doped with Cr, Mn, Fe, Co, Cu, and Zn. The descriptors and catalytic activities were calculated analogously to those in Figure 2. The vertical differences between the red line and the blue lines and/or the points provide an estimation of the oxygen evolution overpotential on the oxides (η_{OER}). a) Effect of doping on Ni sites. It is observed that doping with Mn, Fe, Co, Cu and Zn causes slight increases in the OER overpotential of Ni sites, while Cr causes a slight decrease. b) Activity of dopants in a NiOOH lattice. The overpotentials are rather different depending on the transition metal and Fe and Mn are near the top of the volcano. Pristine NiO (from Figure 2) and IrO_2 (adapted from ref.[18]) are provided for comparison as blue rhombs, while NiOOH appears as a green square.

The noteworthy enhancing effect of Fe on the catalytic activity of nickel hydroxide has been reported in the literature,[13,20,21] although the explanation for such enhancement is still a matter of debate.[13,24,32,46] Although the ligand effect is well known in metal electrocatalysis and has been systematically quantified and exploited,[47,48] the effect of doping in oxide electrocatalysis is less well documented, as its magnitude and direction depends on the interactions between the host and the guest metals in a stretched lattice, in addition to the interactions of the metals and lattice oxygen.[49,50] In our particular case, we observe that the ligand effect is small on Ni sites (Figure 3a), while it is significant on M sites (Figure 3b). This is intuitive, as M is embedded in a lattice where the M-O distances are different from its pure oxide. Furthermore, our results are in agreement with those of Bell and coworkers,[24] who concluded that the metal site responsible for the significant enhancement of the catalytic activity of NiFeOOH compared to NiOOH is Fe, rather than Ni. We predict the same for NiMnOOH, in which Mn will be the active metal. Conversely, in NiCrOOH, which is the other surface that may reduce the OER overpotential, Ni is the active site, rather than Cr, and the enhancement effect should be lower than that of Fe, based on Figure 3a.

It is also important to note that the active sites in Figure 1c possess full coverage of oxygenated species during the OER. Coverage effects are sometimes important, as lateral adsorbate-adsorbate interactions may weaken or strengthen the adsorption energies.[51] The adsorbates covering the surface can be inferred from volcano plots, considering that a) NiOOH is on the weak side of the volcano in Figure 3, so its potential-limiting step is the transformation of *OH into *O, and the Ni sites should be covered with *OH under OER conditions. The situation is analogous for NiCuOOH and NiZnOOH. b) The potential-limiting step for Cr, Mn, Fe and Co monoxides is the transformation of *O into *OOH. Thus, these M sites at NiMOOH surfaces will normally be covered with *O under OER conditions.

Experimentally, one can start assessing the effect of transition metals on NiO-based catalysts by analogy to well-defined mixed oxides. In this vein, Landon *et al.* have proposed that $NiFe_2O_4$ spinel has a significant role in the enhancement of the catalytic

activity of mixed NiFe oxides.[46] The findings of Li and Selloni controvert this statement, as they found through DFT calculations that $NiFe_2O_4$ is active for the OER, but its activity is noticeably lower than that of Fe-doped Ni oxides.[32] To evaluate these conflicting claims, we induced the thermal decomposition of the NiFe DH so as to obtain the spinel structure, as shown in the XRD pattern in Figure C1 in Appendix C, and measured its catalytic activity towards electrochemical water oxidation. The results are summarized in Figure 4, where it is observed that the onset of the reaction on $NiFe_2O_4$ is located at more positive potentials compared to NiFe DH. We conclude, therefore, that the spinel phase is indeed less active than the double hydroxide and that the active sites in both catalysts must be different.

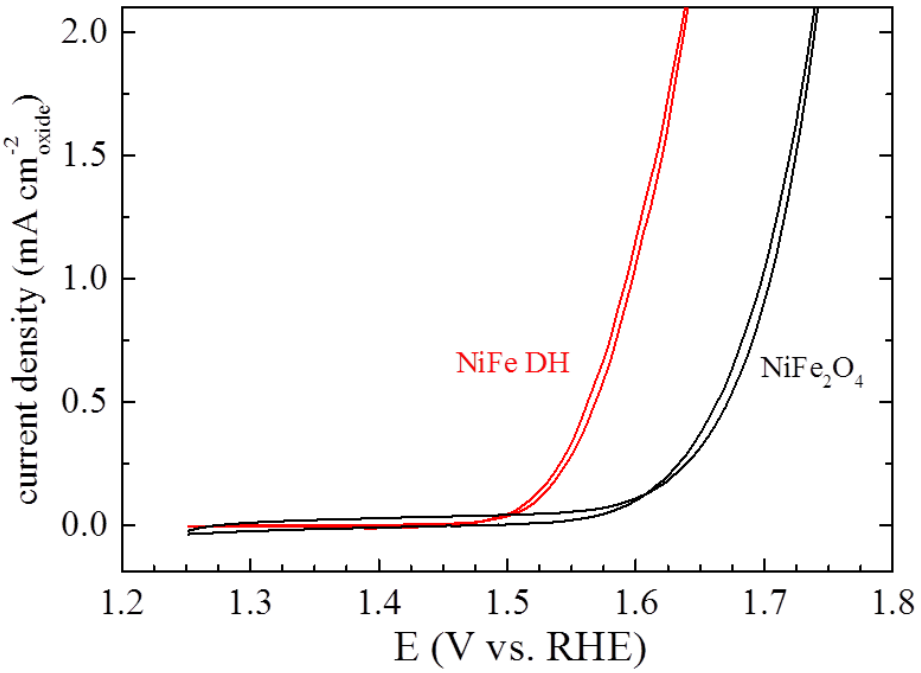

Figure 4. Cyclic voltammetry for the oxygen evolution reaction in 0.1 M KOH of NiFe DH and $NiFe_2O_4$ immobilized on Au. Experiments were performed under hydrodynamic conditions (rotation rate: 1500 RPM, scan rate: 0.01 V s^{-1}). The solid line shows the catalytic activity measured on the NiFe DH and the dashed line shows the activity measured on the $NiFe_2O_4$, obtained after thermal decomposition of the NiFe DH.

The effect of Fe doping on the catalytic activity of NiFe DH was studied for Fe contents in the range 25-75 % (see Figure C3 in Appendix C). We observed that the highest catalytic activity is reached at 50% of Fe doping, so this composition was used to study the doping effects of the other transition metals both experimentally and computationally.

With the theoretical results of Figure 3 in mind, we conducted OER experiments on NiOOH doped with 50% Cr, Mn, Fe, Co, Cu and Zn and on $Ni(OH)_2$, to be used as benchmark. Figure 5 shows the polarization curves obtained for the oxygen evolution on the different catalysts. There is a clear effect of the 3d transition metals in the catalytic activity towards oxygen evolution, measured in terms of current density; in the case of Mn, Cr and Fe, the OER potential to reach 0.5 mA cm^{-2} is reduced by approximately 60, 100 and 130 mV, respectively, compared to $Ni(OH)_2$. On the contrary, Co, Cu and Zn DH's increase the overpotential. Interestingly, NiMn DH is predicted by our theoretical analysis to be as active as NiFe DH. Note, however, that the XRD patterns of the Mn DH (see Figure C2 in Appendix C) suggest that the synthesis method produced a separate phase of $MnCO_3$ and a minor amount of the double hydroxide, which was also confirmed by FTIR measurements (see Figure C4 in Appendix C). Segregation of $MnCO_3$ during the synthesis process may explain the lower than expected catalytic activity observed for the NiMn DH due to a high amount of amorphous sites in the external layers of the hydroxide structure, which are the most catalytically active. It is worth mentioning that the synthesis of the NiCr, NiMn and NiFe was also tried using NaOH as precipitating agent instead of Na_2CO_3 to check the effect of carbonate anion in the catalytic activity of the double hydroxides. Figure C5 in Appendix C shows the polarization curves for OER on the three nickel-based double hydroxide precipitated with sodium hydroxide and sodium carbonate, and it is clear that the catalysts precipitated from Na_2CO_3 have higher OER activity than their counterpart precipitated from NaOH.

Note in passing that in the case of Co-doping, it is observed that $Ni(OH)_2$ segregates from the mixed hydroxide (see Figure C2 in Appendix C). This, however, has no influence in our conclusions, as NiCoOOH is not predicted theoretically to have lower overpotentials than NiOOH.

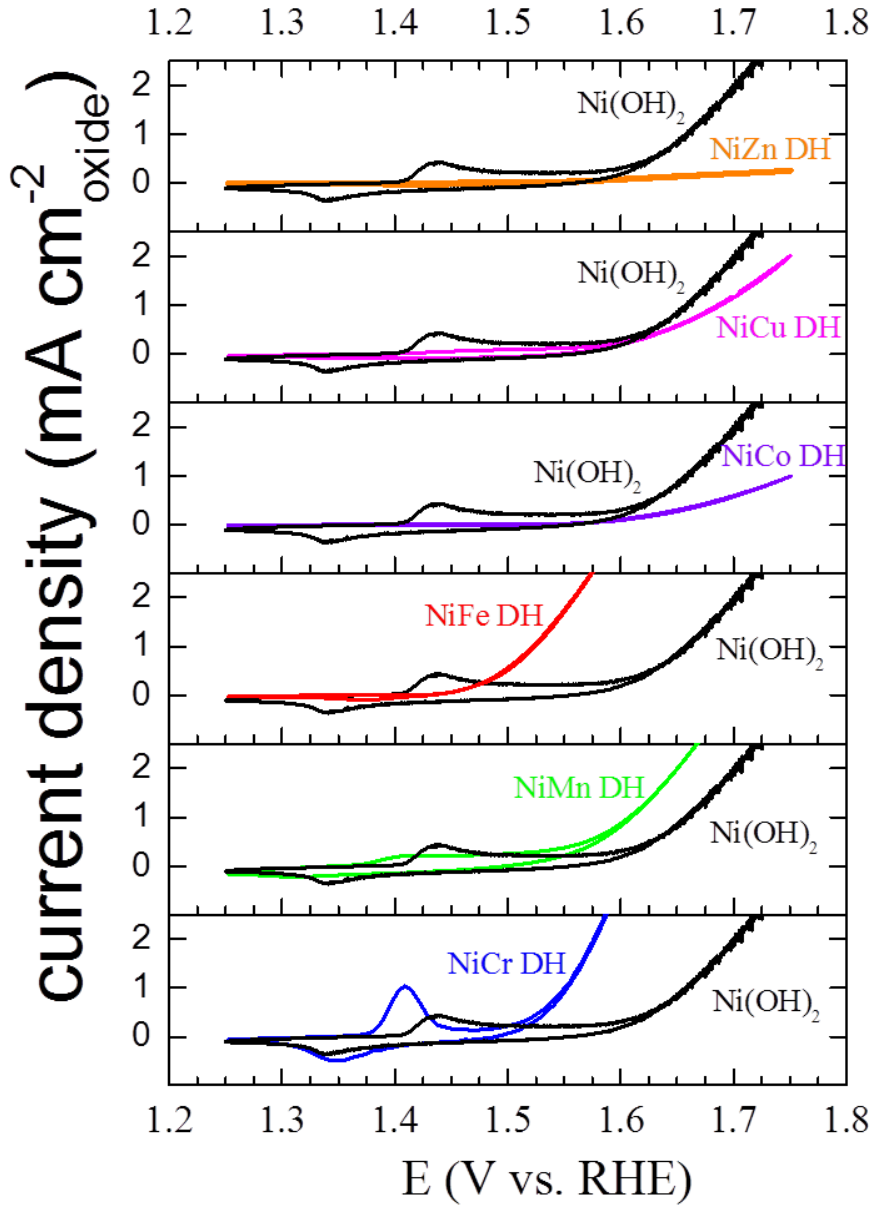

Figure 5. Cyclic voltammetry for the OER in 0.1 M KOH of nickel-based DH immobilized on Au. Experiments were performed under hydrodynamic conditions (rotation rate: 1500 RPM, scan rate: 0.01 V s^{-1}). The solid line shows the activity measured on the DH's and the dashed line shows the activity $Ni(OH)_2$, presented as benchmark of the catalytic activity.

The catalytic activity of the NiFe DH towards electrochemical oxygen evolution in alkaline media was also compared with that of IrO_2, which is normally used as benchmark for this reaction.[12] The double hydroxide possesses higher catalytic activity than the benchmark (see Figure C6 Appendix C) and the activity is comparable to the one reported for NiFe DH supported on carbon nanotubes.[15,22] Importantly, the preparation procedure used in this work is much simpler and can be applied to the elaboration of several other double hydroxides. Such a method might prove advantageous for the large-scale production of catalysts. Moreover, the procedure shows that the enhanced activity of NiFe double hydroxides is mostly due to sites composed of Ni, Fe/Cr and oxygenated species distributed spatially in an octahedral fashion.

We have also estimated the faradaic efficiency towards electrochemical water oxidation catalyzed by NiFe DH by rotating ring-disk electrode (RRDE) measurements.[12] Figure 6 shows that the NiFe catalyst splits water with a faradaic efficiency of >90% at 270 mV of overpotential (see the SI for details about the calculation of the efficiency).

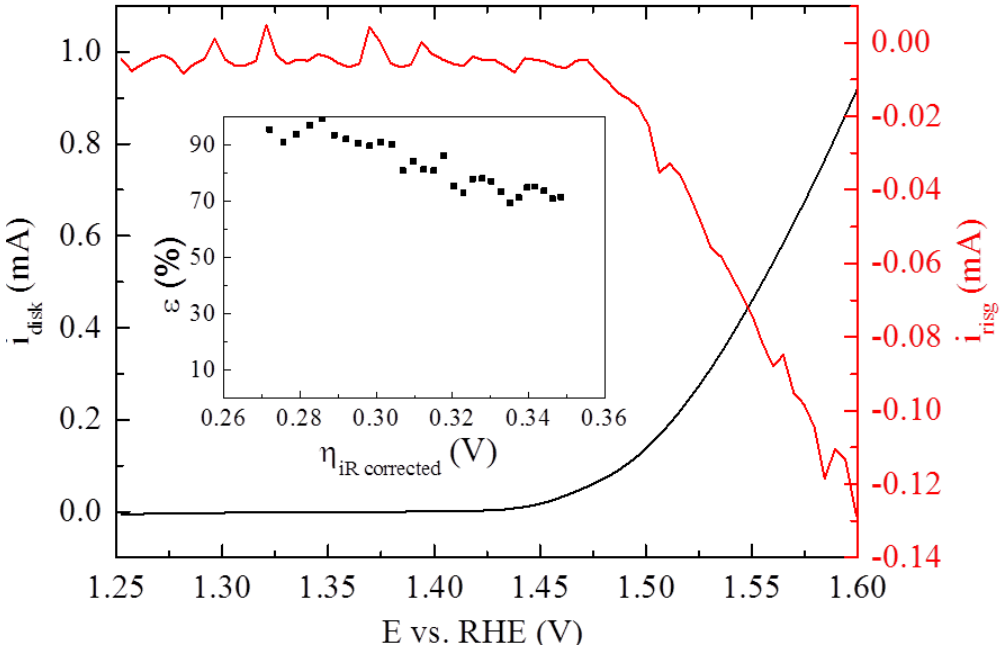

Figure 6. Polarization curve for OER in 0.1 M KOH of nickel-based DH immobilized on Au. Experiments were performed in RRDE configuration (Pt ring at 0.45 V vs. RHE) at 1500 RPM. Scan rate: 0.01 V s^{-1}. Inset: Faradaic efficiency (ε) as function of the potential applied to the disk.

Finally, we have also addressed the important matter of the catalyst stability and durability under working conditions. To do so, we used McCrory *et al.*'s method[12] (further details shown in Appendix C), and conclude that NiFe DHs are more stable than IrO_x nanoparticles, which are typically used as benchmarks.

4.4. Conclusions

We have presented simple guidelines for the rational design of Ni-based double hydroxides with transition metals, to catalyze the electrochemical water oxidation reaction. These rules allowed us to understand the improving effect of Cr, Mn and Fe on the catalytic activity of the Ni-based double hydroxides towards oxygen evolution and the deleterious

effect of Co, Cu and Zn. The active sites are suggested to be of the oxyhydroxide type (that is NiMOOH, where M is a transition-metal dopant), in which the metals form octahedral NiO_6 and MO_6 complexes. We have made one-to-one comparisons between $Ni(OH)_2$ and the double hydroxides, and between the double hydroxides and state-of-the-art IrO_2 nanoparticles. At a reference current density of 0.5 mA cm^{-2} we observed that, on the one hand, Mn, Cr and Fe reduce the potential needed to reach the reference current density by 60 mV, 100 mV and 130 mV with respect to $Ni(OH)_2$. On the other hand, the potential to reach the reference current density is reduced by 160, 190 and 230 mV, compared to IrO_2 nanoparticles, by doping with Mn, Cr and Fe, respectively. These two comparisons show that our simple preparation method renders catalysts that are substantially more active than those in the state of the art. According to the DFT-based analysis presented here, the effects Fe, Mn and Cr doping are different, as Fe and Mn are the active sites in NiFeOOH and NiMnOOH, and Ni is the active site in NiCrOOH.

The NiFe DHs prepared here show significantly higher catalytic activity and stability towards electrochemical water oxidation than IrO_2, with over 90% efficiency for electrochemical O_2 generation. Their activity is comparable to that of NiFe DHs obtained through different procedures, while using a considerably simple preparation method.

These conclusions must be seen in the light of the experimental uncertainty about the exact structure of the surfaces in combination with the accuracy of DFT. Therefore, the significance of this study lies mainly in the guidelines and broader understanding it provides in terms of trends in catalytic activity.

4.5. Acknowledgments

FCV acknowledges funding from the Netherlands Organization for Scientific Research (NWO), Veni project number 722.014.009. This work was also supported by the Netherlands Organization for Scientific Research (NWO) and in part by the BioSolar Cells open innovation consortium, supported by the Dutch Ministry of Economic Affairs, Agriculture and Innovation. The Stichting Nationale Computerfaciliteiten (NCF) is also acknowledged for the use of their supercomputer facilities, with financial support from

NWO. Dr. F. Calle-Vallejo is kindly acknowledged for his computational contributions to the project, and I. Ledezma-Yanez for the assistance with the FTIR characterization of the DHs samples. Prof. Dr. E. Bouwman is acknowledged for the use of the X-Ray Diffraction facility in her group at Leiden University and Dr. W. T. Fu for useful discussions on the XRD results.

REFERENCES

(1) Hoffert, M. I.; Caldeira, K.; Jain, A. K.; Haites, E. F.; Harvey, L. D. D.; Potter, S. D.; Schlesinger, M. E.; Schneider, S. H.; Watts, R. G.; Wigley, T. M. L.; Wuebbles, D. J. *Nature* **1998**, *395*, 881.

(2) Olah, G. A.; Prakash, G. K.; Goeppert, A. *J. Am. Chem. Soc.* **2011**, *133*, 12881.

(3) Crabtree, G. W.; Dresselhaus, M. S.; Buchanan, M. V. *Phys. Today* **2004**, *57*, 39.

(4) McGlade, C.; Ekins, P. *Nature* **2015**, *517*, 187.

(5) Lewis, N. S.; Nocera, D. G. *Proc. Natl. Acad. Sci. U. S. A.* **2006**, *103*, 15729.

(6) Bensaid, S.; Centi, G.; Garrone, E.; Perathoner, S.; Saracco, G. *ChemSusChem* **2012**, *5*, 500.

(7) Hermans, L. J. F. *Energy Survival Guide*; BetaText / Leiden University Press: Amsterdam, 2011.

(8) Koper, M. T. M. *J. Electroanal. Chem.* **2011**, *660*, 254.

(9) Dau, H.; Limberg, C.; Reier, T.; Risch, M.; Roggan, S.; Strasser, P. *ChemCatChem* **2010**, *2*, 724.

(10) Matsumoto, Y.; Sato, E. *Materials Chemistry and Physics* **1986**, *14*, 397.

(11) Lee, Y.; Suntivich, J.; May, K. J.; Perry, E. E.; Shao-Horn, Y. *J. Phys. Chem. Lett.* **2012**, *3*, 399.

(12) McCrory, C. C.; Jung, S.; Peters, J. C.; Jaramillo, T. F. *J. Am. Chem. Soc.* **2013**, *135*, 16977.

(13) Corrigan, D. A. *J. Electrochem. Soc.* **1987**, *134*, 377.

(14) Suntivich, J.; May, K. J.; Gasteiger, H. A.; Goodenough, J. B.; Shao-Horn, Y. *Science* **2011**, *334*, 1383.

(15) Gong, M.; Li, Y.; Wang, H.; Liang, Y.; Wu, J. Z.; Zhou, J.; Wang, J.; Regier, T.; Wei, F.; Dai, H. *J. Am. Chem. Soc.* **2013**, *135*, 8452.

(16) Grimaud, A.; May, K. J.; Carlton, C. E.; Lee, Y. L.; Risch, M.; Hong, W. T.; Zhou, J.; Shao-Horn, Y. *Nat. Commun.* **2013**, *4*.

(17) Song, F.; Hu, X. *Nat. Commun.* **2014**, *5*.

(18) Man, I. C.; Su, H.-Y.; Calle-Vallejo, F.; Hansen, H. A.; Martínez, J. I.; Inoglu, N. G.; Kitchin, J.; Jaramillo, T. F.; Nørskov, J. K.; Rossmeisl, J. *ChemCatChem* **2011**, *3*, 1159.

(19) Oliva, P.; Leonardi, J.; Laurent, J. F.; Delmas, C.; Braconnier, J. J.; Figlarz, M.; Fievet, F.; Guibert, A. d. *J. Power Sources* **1982**, *8*, 229.

(20) Młynarek, G.; Paszkiewicz, M.; Radniecka, A. *J. Appl. Electrochem.* **1984**, *14*, 145.

(21) Corrigan, D. A.; Bendert, R. M. *J. Electrochem. Soc.* **1989**, *136*, 723.

(22) Gong, M.; Dai, H. *Nano Res.* **2014**, 1.

(23) Lu, Z.; Xu, W.; Zhu, W.; Yang, Q.; Lei, X.; Liu, J.; Li, Y.; Sun, X.; Duan, X. *Chem. Commun.* **2014**, *50*, 6479.

(24) Friebel, D.; Louie, M. W.; Bajdich, M.; Sanwald, K. E.; Cai, Y.; Wise, A. M.; Cheng, M.-J.; Sokaras, D.; Weng, T.-C.; Alonso-Mori, R.; Davis, R. C.; Bargar, J. R.; Nørskov, J. K.; Nilsson, A.; Bell, A. T. *J. Am. Chem. Soc.* **2015**, *137*, 1305.

(25) Norskov, J. K.; Bligaard, T.; Rossmeisl, J.; Christensen, C. H. *Nat. Chem.* **2009**, *1*, 37.

(26) Kresse, G.; Furthmüller, J. *Phys. Rev. B* **1996**, *54*, 11169.

(27) Hammer, B.; Hansen, L. B.; Nørskov, J. K. *Phys. Rev. B* **1999**, *59*, 7413.

(28) Vanderbilt, D. *Phys. Rev. B* **1990**, *41*, 7892.

(29) Methfessel, M.; Paxton, A. T. *Phys. Rev. B* **1989**, *40*, 3616.

(30) Calle-Vallejo, F.; Koper, M. T. M. *Electrochim. Acta* **2012**, *84*, 3.

(31) Nørskov, J. K.; Rossmeisl, J.; Logadottir, A.; Lindqvist, L.; Kitchin, J. R.; Bligaard, T.; Jónsson, H. *J. Phys. Chem. B* **2004**, *108*, 17886.

(32) Li, Y.-F.; Selloni, A. *ACS Catal.* **2014**, *4*, 1148.

(33) Cavani, F.; Trifirò, F.; Vaccari, A. *Catal. Today* **1991**, *11*, 173.

(34) Suntivich, J.; Gasteiger, H. A.; Yabuuchi, N.; Shao-Horn, Y. *J. Electrochem. Soc.* **2010**, *157*, B1263.

(35) Grimaud, A.; May, K. J.; Carlton, C. E.; Lee, Y.-L.; Risch, M.; Hong, W. T.; Zhou, J.; Shao-Horn, Y. *Nat Commun* **2013**, *4*.

(36) Suntivich, J.; May, K. J.; Gasteiger, H. A.; Goodenough, J. B.; Shao-Horn, Y. *Science* **2011**, *334*, 1383.

(37) Trasatti, S.; Petrii, O. A. *Journal of Electroanalytical Chemistry* **1992**, *327*, 353.

(38) McFarland, E. W.; Metiu, H. *Chem. Rev.* **2013**, *113*, 4391.

(39) Calle-Vallejo, F.; Díaz-Morales, O. A.; Kolb, M. J.; Koper, M. T. M. *ACS Catal.* **2015**, 869.

(40) Calle-Vallejo, F.; Inoglu, N. G.; Su, H.-Y.; Martinez, J. I.; Man, I. C.; Koper, M. T. M.; Kitchin, J. R.; Rossmeisl, J. *Chem. Sci.* **2013**, *4*, 1245.

(41) Trasatti, S. *Electrochim. Acta* **1984**, *29*, 1503.

(42) Bajdich, M.; García-Mota, M.; Vojvodic, A.; Nørskov, J. K.; Bell, A. T. *J. Am. Chem. Soc.* **2013**, *135*, 13521.

(43) Chen, J.; Selloni, A. *J. Phys. Chem. C* **2013**, *117*, 20002.

(44) Diaz-Morales, O.; Calle-Vallejo, F.; de Munck, C.; Koper, M. T. M. *Chemical Science* **2013**, *4*, 2334.

(45) Kurth, S.; Perdew, J. P.; Blaha, P. *Int. J. Quantum Chem* **1999**, *75*, 889.

(46) Landon, J.; Demeter, E.; İnoğlu, N.; Keturakis, C.; Wachs, I. E.; Vasić, R.; Frenkel, A. I.; Kitchin, J. R. *ACS Catal.* **2012**, *2*, 1793.

(47) Calle-Vallejo, F.; Koper, M. T. M.; Bandarenka, A. S. *Chem. Soc. Rev.* **2013**, *42*, 5210.

(48) Kitchin, J. R.; Nørskov, J. K.; Barteau, M. A.; Chen, J. G. *Phys. Rev. Lett.* **2004**, *93*, 156801.

(49) Gelatt, C. D.; Williams, A. R.; Moruzzi, V. L. *Phys. Rev. B* **1983**, *27*, 2005.

(50) Calle-Vallejo, F.; Martínez, J. I.; García-Lastra, J. M.; Mogensen, M.; Rossmeisl, J. *Angew. Chem. Int. Ed.* **2010**, *49*, 7699.

(51) Grabow, L.; Hvolbæk, B.; Nørskov, J. *Top. Catal.* **2010**, *53*, 298.